RESEARCH ARTICLE

An Optimized Alternative Fixed Switching 12-Sector Space Vector Pulse Width Modulation Control of Open-End Winding PMSM Drive

BERHANU DEGGEFA LEMMA [ID][1,2] AND SRINIVASAN PRADABANE[1]
[1]Department of Electrical Engineering, National Institute of Technology at Warangal, Warangal, Telangana 506004, India
[2]Department of Electrical Engineering, Dire Dawa University, Dire Dawa 1362, Ethiopia

Corresponding author: Berhanu Deggefa Lemma (bezakiyya@gmail.com)

ABSTRACT Over the past few years, there has been an increase in the use of open-end winding (OEW) PMSM applications. The fault tolerance of the topology makes OEW PMSM suitable for various intermittent operations. However, a dual inverter operation causes OEW PMSM drive schemes to exhibit high commutation and ripple. This paper presents an optimized alternative fixed switching 12-sector space vector pulse width modulation (svpwm) control for open-end winding PMSM drives. This work reduces the commutation number without compromising drive system performance. In comparison with conventional 6-sector svpwm, this control scheme offers three advantages. It incorporates optimal signal generation, a virtual state method for segmenting sectors into small sectors, and alternative fixed switching methods based on sub-hexagons. Inverters are assigned fixed voltage states based on sub-hexagon numbers. The proposed scheme was validated in the Matlab2021b Simulink environment. Based on the simulation results, it is found that the proposed scheme is effective for OEW PMSM. Finally, OPAL-RT (OP4500) is used to verify scheme effectiveness. The verification of the proposed scheme indicates its effectiveness. Results obtained from real-time hardware have ripple of 1.25% and 5% for speed and torque performance, respectively.

INDEX TERMS Fixed switching, OEW-PMSM, MTPA, svpwm, virtual state.

I. INTRODUCTION

Several applications, including electric vehicles, can be benefit from PMSMs' compact design and efficiency. Though PMSM is highly efficient, it has drawbacks, like cogging torque and ripples. These cause mechanical and electrical failures. Cogging torque leads to vibration and wear. Whereas a harmonic torque leads to overheating and noise. With open-end windings (OEWs), different voltage levels can be provided based on the ratio of the voltages on the two sides.

Additionally, OEW PMSM can overcome the ripple when a fault occurs on just one inverter switch or arm. This led to the emergence of the OEW scheme as the solution to the problems associated with high ripple caused by faults. Multi-level inverters have revolutionized high-power and

The associate editor coordinating the review of this manuscript and approving it for publication was Atif Iqbal [ID].

superior-performance industrial drive applications. In addition to being easier to implement digitally, svpwm utilizes a DC bus more efficiently and has a lower THD [1].

Combining the benefits of svpwm and direct torque control minimizes torque ripple. The advantage of reducing ripple is obtained from the good steady-state performance of svpwm. The optimal vector sequence approach reduces the harmonics performance of classical svpwm further. Selective harmonic rejection reduces the magnitude of lower-order harmonics. For 11 pulses under fully loaded conditions, harmonics are minimized in [2]. Significant factors in PMSM torque and ripple performance are the number of commutated switches, the accuracy of control signal estimation, and the timing of each switch. Optimum control signal estimation and commutated switch reduction can minimize these problems. In [3], a three-level svpwm algorithm was proposed. The scheme works like the two-level method. In addition to other performances, svpwm reduces voltage waveform distortion [4].

An algorithm for estimating switching time using layers is presented in the paper [5]. As a means of calculating switching time, a large hexagon is divided into several smaller hexagons. Obtaining on-time is easy with svpwm when it is dissolved into two-level modulation. A simple svpwm based on instantaneous voltage samples has been proposed in [6]. Zero sequence voltage reduction has a significant impact on motor reliability [7]. It is necessary to apply a voltage equivalent to the negative magnitude of the zero-sequence current to eliminate the positive magnitude zero-sequence current and vice versa if the current is positive. As shown in [8], the OEW PMSM is controlled through single-phase commutation. In this work, only one phase is switched per switching period to reduce commutation. The special control is needed for one-phase switches to control torque and speed. The current magnitude needs to be modified. With this modification, the required response can be achieved via a single-phase current rather than a 3-phase current. In [9], the authors examined the performance of OEW PMSM systems powered by a dual inverter used in electric traction applications. In order to ensure compatibility, OEW PMSM schemes supplied by dual inverters were compared with PMSM schemes supplied by single inverters. Modulation approaches were proposed in [10] and [11] to utilize svpwm modulation to minimize the common mode voltage and sub-harmonic. A virtual vector was proposed to reduce the complexity of the svpwm algorithm in [12].

3D-svpwm reduces the algorithm complexity and provides the advantages of 2D-svpwm [13]. A novel svpwm without considering a level number has been proposed in [14] to reduce reference signal computation. A higher voltage level results in better ripple performance. The modern drive scheme uses multi-level voltage and OEW to achieve higher torque and reliability. A benefit of OEW schemes is that the DC link ratio between the two side inverters can be adjusted to increase the voltage level at the output [15]. The works in [16] and [17] describe an OEW PMSM control system using two inverters with different DC voltages. In [18], it is suggested that OEW PMSM drives can achieve improved ripple performance by reducing their current suppression under faulty conditions. A unified scheme uses the two terminal voltages to determine the active voltage state of both inverters. This is unlike the opposite scenario, where one inverter is used for supply and the other for clamping [19]. The commutation reduction scheme of OEW PMSM was presented in [20]. In order to achieve this, the switching period is synchronized. The work in [21] discusses the methodology for eliminating the zero-sequence current in OEW PMSM controlled by the svpwm. By applying a voltage based on the zero-sequence current's sign, the zero-sequence current can be eliminated.

An OEW PMSM with multi-level feed is presented in [22] and [23]. The purpose of this scheme is to improve output. In order to reduce zero-sequence current, the neutral voltage must be balanced. A neutral balancing is achieved by dispersing the reference voltage equally between two inverters. Adding half the difference to the lower magnitude reference

value and subtracting half from the higher magnitude reference value will yield neutral balancing [24]. The reconfigured scheme is described in [25] for suppressing common mode voltages and enhancing the reliability of an OEW-PMSM, which is fed by an inverter. The svpwm with zero-sequence current control is proposed for OEW PMSM in [26]. A reduction in zero sequence current can be achieved by only using the active voltage state. A PMSM vector control scheme based on svpwm is proposed for OEW PMSM in [27].

This paper presents an optimal alternative fixed switching 12-sector svpwm control for the OEW PMSM drive. The three main advantages of this control scheme are stated as follows. First, a simple MTPA algorithm is used to optimize the current magnitude. Additionally, this control scheme uses an effective 12-sector approach to segment the sectors to determine dwelling times. Sector segmentation is based on linear averages. Alternate fixed switching schemes generate one inverter switching signal per mini hexagon using svpwm and another by static switching. With the proposed scheme, ripple is reduced by commutation reduction, and efficiency is improved by MTPA. In this work, PMSM modeling is first described, followed by OEW PMSM and its control scheme. Finally, the report includes simulation results, experimental verification of the proposed scheme with OPAL-RT, and a conclusion.

II. PMSM MATHEMATICAL MODEL

A simplified d-q axis model is used to represent PMSM. The expression *xq* indicates the magnitude of the q-axis of variable *x*. The variables V, i, ψ, and ω_s are voltage, current, flux, and synchronous speed, respectively.

$$\begin{cases} V_q = R \times i_q + \dfrac{d\psi_q}{dt} + \omega_s \times \psi_d \\ V_d = R \times i_d + \dfrac{d\psi_d}{dt} - \omega_s \times \psi_q \end{cases} \quad (1)$$

The flux magnitude is obtained as shown below when *mf* is magnet flux.

$$\begin{cases} \psi_{sd} = L_d \times i_d + m_f \\ \psi_{sq} = L_q \times i_q \end{cases} \quad (2)$$

Current is derived from (1) as shown below when L is inductance.

$$\begin{cases} i_q = \dfrac{1}{Lq} \displaystyle\int \left[V_q - R \times i_q - \omega_s \times \psi_d \right] dt \\ i_d = \dfrac{1}{L_d} \displaystyle\int \left[V_d - R \times i_d + \omega_s \times \psi_q \right] dt \end{cases} \quad (3)$$

While the torque and speed of a motor are expressed as shown below. When the variable P_n is pole number, *Te* developed torque, T_L is load, J is the moment of inertia of the rotor, B friction coefficient of the motor, and ω_r is the mechanical speed of the rotor.

$$\begin{cases} T_e = 1.5 \times P_n \left(\psi_{sd} \times i_q - \psi_{sq} \times id \right) \\ \omega_r = \dfrac{1}{J} \displaystyle\int (T_e - T_L - B \times \omega_r) dt \end{cases} \quad (4)$$

III. AN OVERVIEW OF OEW PMSM AND THE PROPOSED CONTROL SCHEME

A general representation of an optimized 12-sector svpwm for driving the OEW PMSM drive is depicted in Fig. 1.
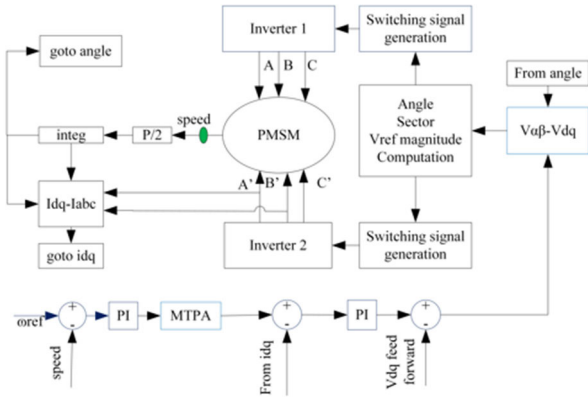

FIGURE 1. Layout of the proposed control system.

In this study, a constant parameter approach maximum torque per ampere is used to generate optimal current. Based on the voltage difference between two terminals in a phase winding, the net voltage for each phase of an OEW PMSM is calculated. This equation determines the magnitude of the voltages generated by both inverters based on their magnitudes of DC voltages and the switching signals for both inverters. Thus, one has to change the ratio between the DC links of both inverters to alter the magnitude of the voltage [28]. The variables SA, SB, and SC represent phase A, phase B, and phase C upper switch switching signals respectively for the first inverter. The variables SA′, SB′, and SC′ represent phase A, phase B, and phase C upper switch switching signals for the second inverter respectively.

$$
\begin{cases}
VAA' = SA \times Vdc1 - SA' \times Vdc2 \\
VBB' = SB \times Vdc1 - SB' \times Vdc2 \\
VCC' = SC \times Vdc1 - SC' \times Vdc2
\end{cases}
\tag{5}
$$

In the following expression, the objective function and constraint approach are used to define MTPA.

$$
\begin{cases}
objective\ function, \quad i_s = \sqrt{i_d{}^2 + i_q{}^2} \\
Constraint, \quad T_e = 1.5 \times P_n \times \left(\psi_{sd} \times i_q - \psi_{sq} \times id\right)
\end{cases}
\tag{6}
$$

Using permanent magnet flux in combination with current, the optimal current magnitude was determined. Intermediate variables χ and $i\chi$ are defined as shown below.

$$
\begin{cases}
\chi = \dfrac{mf}{2 \times (L_q - L_d)} \\
i\chi = i_q - \mathrm{sgn}(i_q) \times i_d
\end{cases}
\tag{7}
$$

With the intermediate variables given in (7), it was possible to find the optimal current on the d-q axis by using the

following formula.

$$
\begin{cases}
i_q = i\chi + \mathrm{sgn}(i\chi) \times id \\
id = \dfrac{-i\chi^2}{2\left[\chi + i\chi \times \mathrm{sgn}(i\chi)\right]}, \quad for\ i\chi \neq 0 \\
else, \quad id = 0,\ for\ i\chi = 0
\end{cases}
\tag{8}
$$

A reference voltage is equal to the difference between the references of two inverters. Reference voltages for inverters are expressed as follows.

$$
V_{\alpha\beta\mathrm{ref}} = V1_{\alpha\beta\mathrm{ref}} - V2_{\alpha\beta\mathrm{ref}}
\tag{9}
$$

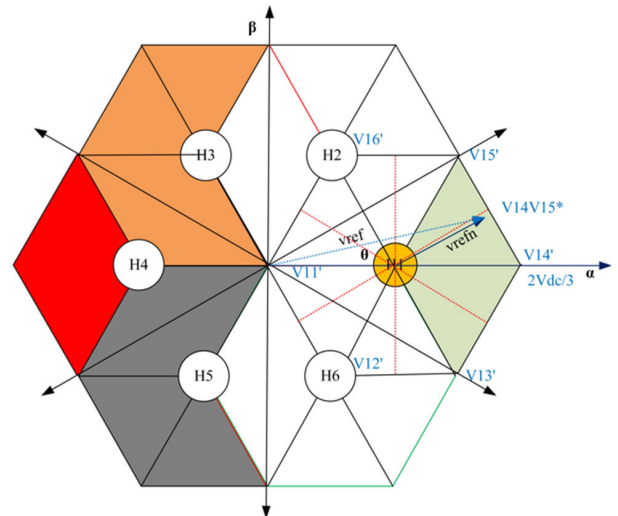A pair of independent switching signals are used by the OEW.

FIGURE 2. Depicts the dissolution of 3-level to 2-level svpwm.

Both inverters' switching is done based on their respective reference voltages. Both inverter states together result in 8*8 states. There are six sub-hexagons within the main hexagon. Sub-hexagon centers are indicated by the variables H1, H2, H3, H4, H5, and H6. A sub-hexagon is selected in accordance with the angle of the original reference voltage. By taking the difference between the reference voltage and the sub-hexagon center, the new reference voltage is determined. An angle, sub-hexagon, and reference voltage relationship are shown in Table 1. In Table 1, β and α indicate $vref \times cos(\theta)$ and $vref \times sin(\theta)$, respectively.

The magnitude of the new reference voltage and angle is determined as shown below.

$$
\begin{cases}
V_{refn} = \sqrt{V_{\alpha ref}{}^2 + V_{\beta ref}{}^2} \\
\theta = \tan^{-1}\left(V_{\beta ref}/V_{\alpha ref}\right)
\end{cases}
\tag{10}
$$

TABLE 1. Calculation of sub-hexagon voltages.

Angle	H	Vαref	Vβref
-30<θ<30	1	β-2Vdc/3	α
30<θ<90	2	β-Vdc/3	α-(√3Vdc)/3
90<θ<150	3	β+Vdc/3	α-(√3Vdc)/3
150<θ<210	4	β+2Vdc/3	α
210<θ<270	5	β+Vdc/3	α+(√3Vdc)/3
270<θ<330	6	β-Vdc/3	α-(√3Vdc)/3

If Ts is the switching period, and n is the sector number. The following formula is used to calculate dwelling time.

$$\begin{cases} T_1 = \dfrac{3 \times V_{refn} \times T_s \times \sin(npi/6 - \theta)}{Vdc \times \sin(pi/6)} \\ T_2 = \dfrac{3 \times V_{refn} \times T_s \times \sin(\theta - (n-1)pi/6)}{Vdc \times \sin(pi/6)} \end{cases} \quad (11)$$

The 12-sector svpwm switches have a switching state of 0.5, which means that the switch remains on and off during half of the switching time. Sub-hexagon 1, with the angle 0 to 30 degrees for the Vref shown in Fig. 2, has two active states: V14* and V14*V15*. In this case, xy indicates the linear average of x and y. For the first inverter, both switching states are (1,0,0). For the second active voltage of the second inverter, the linear average of V4*(0,1,1) and V5*(0,0,1) is (0,0.5,1). Hence, for the second inverter, the switching states are (0,0.5,1) and (001). This means the second switch remains in the on and off position for half the switching period. Commutation numbers are reduced by applying alternative fixed states based on sub-hexagon numbers [29]. Fig. 3 shows the switching signal for H1 and H2.
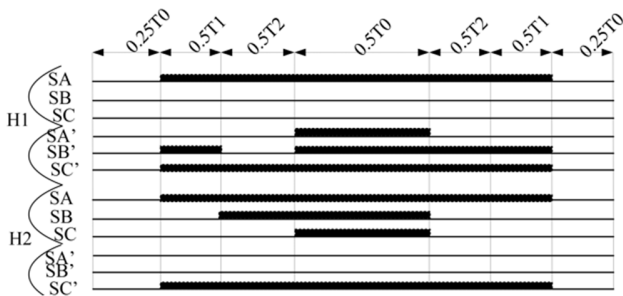

FIGURE 3. Switching signal of inverter in sector one of mini hexagon H1 and H2.

Inverter 1 switching signal is kept constant in H1. On the other hand, the switching signal of the second inverter is determined by dwell time. In Table 2, xy represents the linear average of x and y. This means V12 is a linear average of V1 and V2. Voltage states are selected using the scheme stated in Table 2. There is one constant state inverter in one sub-hexagon and one switched state inverter in the other. In sub-hexagon H1, for example, the first inverter has an active voltage of V1.

TABLE 2. Voltage state selection.

sector	Sub-hexagon		
	H1	H2	H3
	Inverter1=V1	Inverter2 =V5	Inverter1=V3
1	V7V4V45V8	V7V1V12V8	V7V4V45V8
2	V7V45V5V8	V7V12V2V8	V7V45V5V8
3	V7V5V56V8	V7V2V23V8	V7V5V56V8
4	V7V56V6V8	V7V23V3V8	V7V56V6V8
5	V7V6V61V8	V7V3V34V8	V7V6V61V8
6	V7V61V1V8	V7V34V5V8	V7V61V1V8
7	V7V1V12V8	V7V5V56V8	V7V1V12V8
8	V7V12V2V8	V7V56V6V8	V7V12V2V8
9	V7V2V23V8	V7V6V61V8	V7V2V23V8
10	V7V23V3V8	V7V61V1V8	V7V23V3V8
11	V7V3V34V8	V7V1V12V8	V7V3V34V8
12	V7V34V4V8	V7V12V1V8	V7V34V4V8
sector	Sub-hexagon		
	H4	H5	H6
	Inverter2=V1	Inverter1=V5	Inverter2=V3
1	V7V1V12V8	V7V4V45V8	V7V1V12V8
2	V7V12V2V8	V7V45V5V8	V7V12V2V8
3	V7V2V23V8	V7V5V56V8	V7V2V23V8
4	V7V23V3V8	V7V56V6V8	V7V23V3V8
5	V7V3V34V8	V7V6V61V8	V7V3V34V8
6	V7V34V5V8	V7V61V1V8	V7V34V5V8
7	V7V5V56V8	V7V1V12V8	V7V5V56V8
8	V7V56V6V8	V7V12V2V8	V7V56V6V8
9	V7V6V61V8	V7V2V23V8	V7V6V61V8
10	V7V61V1V8	V7V23V3V8	V7V61V1V8
11	V7V1V12V8	V7V3V34V8	V7V1V12V8
12	V7V12V1V8	V7V34V4V8	V7V12V1V8

TABLE 3. Simulation data.

Para	Magnitude	Para	Magnitude
Lq	24.4 mH	Vdc2	110 Volt
speed	1500 rpm	frequency (fs)	1 kHz
Ld	21.3 mH	Flux (mf)	0.725 Wb
Pole	4	Resistance	1.12 Ohm
Vdc1	220 Volt	Rated torque	23 Nm

IV. SIMULATION AND RESULTS

A Matlab-2021b was used to perform the simulation. The simulation parameters are presented in Table 3.

The diagrams in Fig. 4 and Fig. 5 show the switching signal for both sides of the inverters taken for a time span of 0.5 seconds. The signal shown in Fig. 4 represents the switching signal for inverter 1. On the diagram in Fig. 4, SAU, SAL, SBU, SBL, SCU, and SCL represent phase A upper switch switching signal, phase A lower switch switching signal, phase B upper switch switching signal, phase B lower switch switching signal, phase C upper switch switching signal, and phase C lower switch switching signal respectively. In Fig. 5,
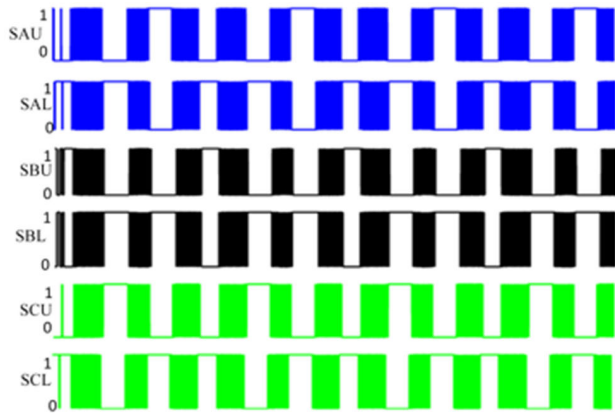
you can see the switching signal for inverter 2. On the diagram in Fig. 5, SA′U, SA′L, SB′U, SB′L, SC′U, and SC′L represent phase A upper switch switching signal, phase A lower switch switching signal, phase B upper switch switching signal, phase B lower switch switching signal, phase C upper switch switching signal, and phase C lower switch switching signal respectively.

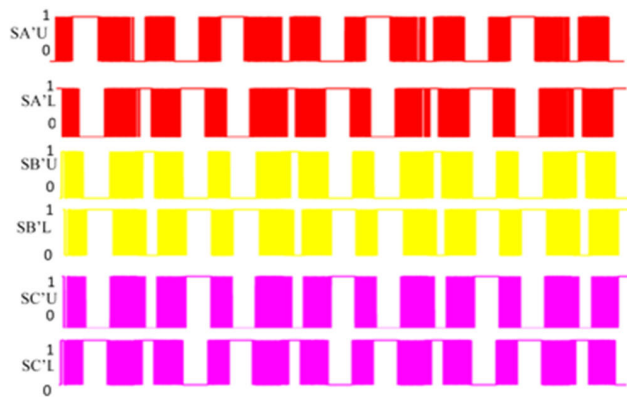**FIGURE 4.** Switching signal for inverter 1.

FIGURE 5. Switching signal for inverter 2.

The simulation was divided into four parts. Simulations were conducted by considering a fully loaded drive running at low speed for 0 to 0.5 seconds. Once again, a fully loaded motor with high-speed operation was observed for a period of 0.5 to 1 second. Between 1 second and 1.5 seconds, the torque was reduced to see how lightly loaded motors performed at high speed. Finally, lightly loaded conditions at low speeds were considered between 1.5 and 2 seconds. In Fig. 6 (a), the speed ripple varies between 416 to 420 *rpm* and 237 to 239 *rpm* in the time ranges of 0.8 to 0.95 seconds and 1.6 to 1.65 seconds. The speed ripple is calculated as a percentage using the following formula.

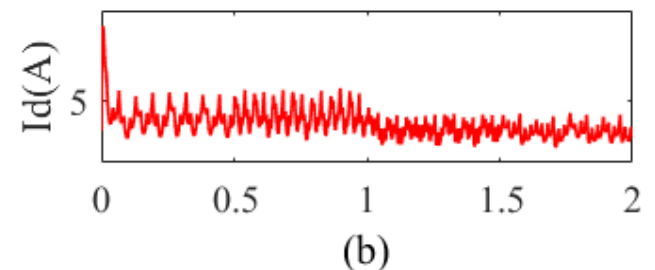$$\%ripple = \frac{0.5(max - min)}{0.5 * (min + max)} \times 100 \qquad (12)$$
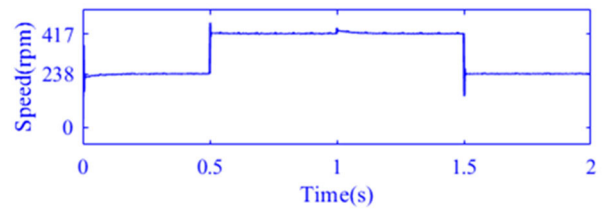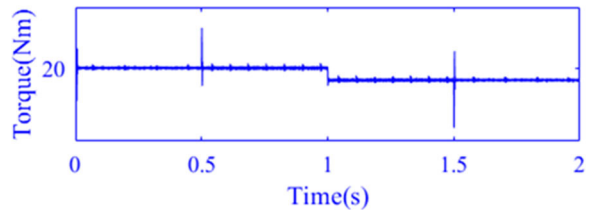
FIGURE 6. (a) Speed and (b) torque response.
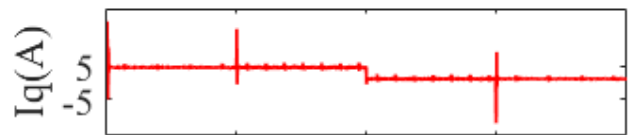
FIGURE 7. (a) Shows the q-axis current, and (b) is the d-axis current.

The high-speed ripple percent is 0.478%, and the low-speed ripple percent is 0.420%, based on equation (12). In Fig. 6(b), between 0.7 and 0.9 seconds, the torque ripple varies from 20.5 to 19.5 *Nm*. There is a ripple of 2.5% in torque. Fig. 6 (b) and Fig. 7 (a) show that the q-axis current has a significant effect on torque developed by torque. On the other hand, as shown in the diagram in Fig. 7 (a) and Fig. 8 (b), the magnitude and ripple in the d-axis current have a direct effect on flux magnitude and flux ripple performance. The result in the diagram shown in Fig. 7 (a) has a ripple magnitude of 6.67% in a lower speed range.

In Fig. 8, the stator current and flux magnitude are presented at different loading levels. Fig. 9 (a) shows the current THD for a highly loaded motor at 238 *rpm* and 20 *Nm* of torque.

THD is measured at t = 0.2 seconds for the low-speed range and at 0.9 seconds for the high-speed
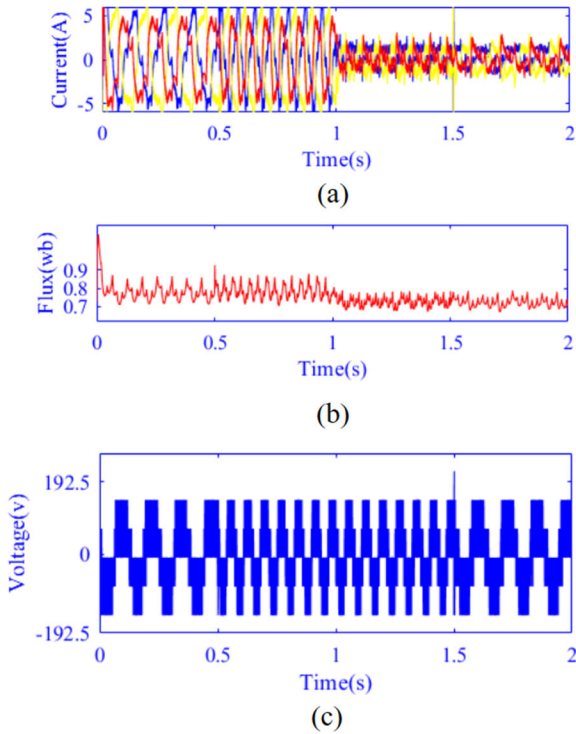
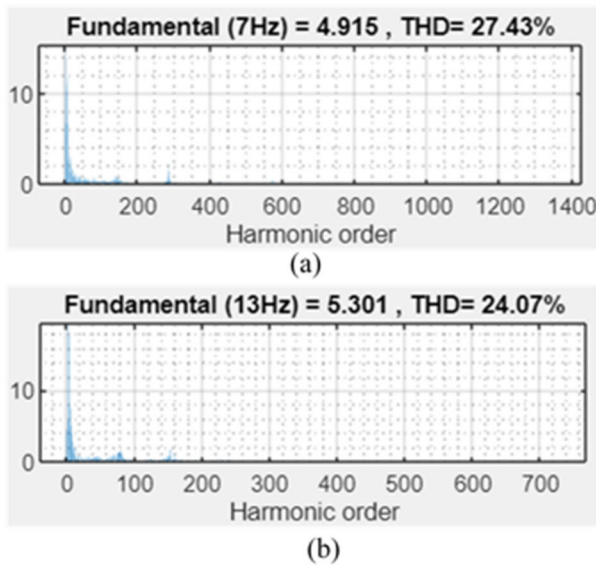FIGURE 8. (a) Shows the current and (b) is a flux waveform, and (c) is voltage.

FIGURE 9. (a) Corresponds to THD at 238 rpm and 20 Nm, whereas (b) corresponds to THD at 417 rpm and 20 Nm.

range, respectively.

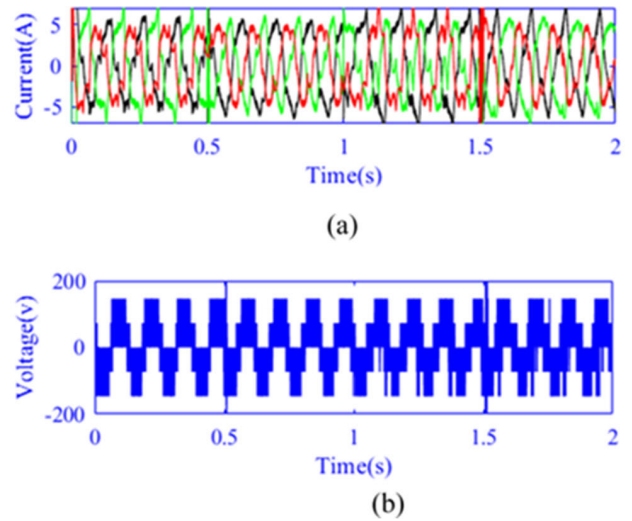$$I_{THD} = \frac{\sqrt{\sum\limits_{n=2}^{\infty} I_n^2}}{I_1} \qquad (13)$$

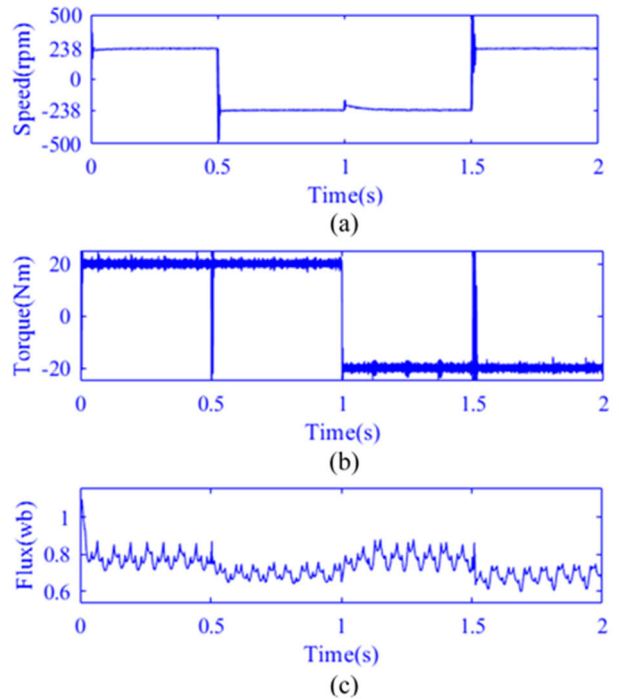FIGURE 10. (a) Current and (b) voltage four quadrant operation.

FIGURE 11. Shows performance in four-quadrant operation, (a) shows speed, (b) shows torque, and (c) shows flux response.

The harmonic component sum can be calculated in the following way.

$$(I_{THD} \times I_1)^2 = \sum_{n=2}^{\infty} I_n^2 \qquad (14)$$

The harmonic level measures how much power is lost due to harmonics. In order to compare harmonic power loss to total power loss, the following formula can be used.

$$\frac{P_{lossh}}{P_{lossT}} = \frac{(I_{THD} \times I_1)^2}{(I_{THD} \times I_1)^2 + I_1^2} = \frac{(I_{THD})^2}{(I_{THD})^2 + 1} \qquad (15)$$
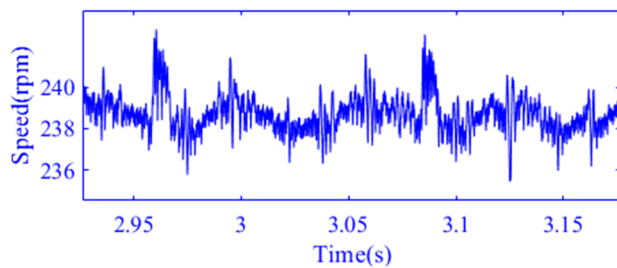
FIGURE 12. Real-time simulator setup.

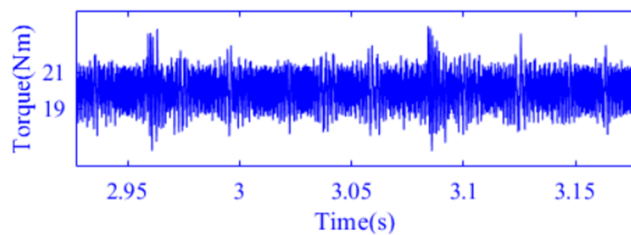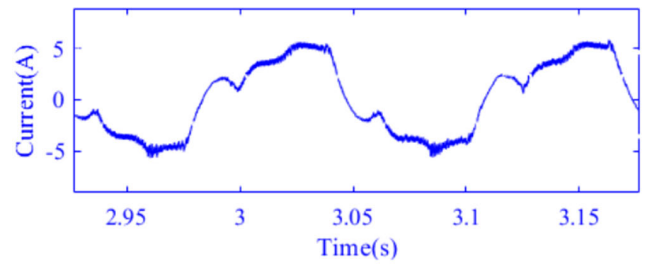**FIGURE 13.** Speed response results obtained from the simulator.

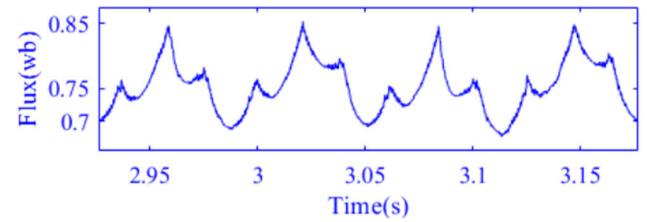

FIGURE 14. Torque results obtained from the simulator.

FIGURE 15. (a) Current and (b) flux.
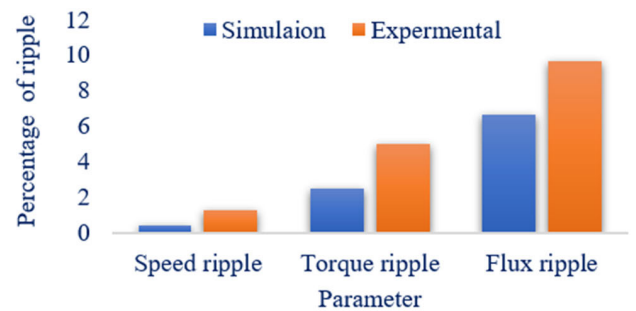
FIGURE 16. Shows the comparison of simulation and real-time simulator results.

In this simulation, the harmonic power loss ratio is 7.55 percent at 238 *rpm* and 5.86 percent at 417 *rpm* for the motor at 20 *Nm* load. Fig. 10 shows the drive's performance in four quadrants using a proposed control scheme.

In general, the simulation results from Fig. 6 and Fig. 11 indicate the scheme is effective. The diagram in Fig. 6 indicates that the speed and torque ripple of this control scheme is good. Fig. 7 indicates that to have less torque ripple, focusing on q-axis current control is important. In addition, the flux magnitude has a great effect on the speed ripple. Especially for a wide speed range, control over flux has a significant influence. Simulation results in Fig. 10 and Fig. 11 indicate the four-quadrant operation. Fig. 11 (a) and Fig. 11 (b) demonstrate that speed and torque ripple is small in all quadrants. Whereas the diagram in Fig. 11 (c) shows that flux ripple is also good.

This control scheme produces effective performance in all four quadrants.

V. EXPERIMENTAL VERIFICATION

Control scheme effectiveness was tested with HIL. In order to compile and run the model on OPAL-RT (OP4500), Matlab 2018a and RT-Lab 2021.3 were used.

Fig. 13, Fig. 14, and Fig. 15 illustrate the results obtained from the setup. The diagram in Fig. 13 shows the speed response. As shown in Fig. 13, the ripple magnitude is 1.25% if (12) is used for ripple computation. The proposed scheme significantly reduces ripple speed.

Fig. 14 shows simulation results for torque. Based on equation (12), the ripple magnitude obtained from the simulator is 5%. On the other hand, Fig. 15 shows the waveform for current and flux. Based on equation (12), the simulator results indicate a ripple magnitude of 9.67% is obtained for a flux.

The result in Fig. 13 to Fig. 15 also indicates the verification of the scheme with OPAL-RT(OP4500). The results indicate that the scheme is effective.

VI. COMPARISONS OF EXPERIMENTAL AND SIMULATION RESULTS

Simulation and experimental results indicate that the proposed scheme reduces speed, torque, and flux ripples. The difference between the simulation and experimental results is that the real-time simulator simulates the system's actual behavior. There is a small difference between the two results. The diagram in Fig. 16 shows the ripple performance of the proposed scheme.

VII. CONCLUSION

An optimized alternative fixed switching 12-sector pulse width modulation control for open-end winding PMSM drives is presented in this paper. The effectiveness of the proposed scheme is tested for variable torque, variable speed, and four-quadrant operation. Simulation results indicate that the speed ripple is very small in both the high and low-speed ranges. The simulation results for the four-quadrant operation also indicate that the scheme is effective for the four-quadrant operation. In addition, OPAL-RT (OP4500) verification shows the scheme to be effective. The OPAL-RT test results showed that the proposed scheme had superior performance, especially speed and torque ripple.

REFERENCES

[1] Z. B. Ibrahim, M. D. L. Hossain, M. H. N. Talib, R. Mustafa, and N. M. N. Mahadi, "A five level cascaded H-bridge inverter based on space vector pulse width modulation technique," in *Proc. IEEE Conf. Energy Convers. (CENCON)*, Oct. 2014, pp. 293–297, doi: 10.1109/CENCON.2014.6967518.

[2] A. Tripathi and G. Narayanan, "Investigations on optimal pulse width modulation to minimize total harmonic distortion in the line current," *IEEE Trans. Ind. Appl.*, vol. 53, no. 1, pp. 212–221, Jan. 2017, doi: 10.1109/TIA.2016.2614630.

[3] H. W. van der Broeck, H.-C. Skudelny, and G. V. Stanke, "Analysis and realization of a pulsewidth modulator based on voltage space vectors," *IEEE Trans. Ind. Appl.*, vol. 24, no. 1, pp. 142–150, Jan. 1988, doi: 10.1109/28.87265.

[4] K. C. Jana, S. K. Biswas, and P. Thakura, "A simple and generalized space vector PWM control of cascaded H-bridge multilevel inverters," in *Proc. IEEE Int. Conf. Ind. Technol.*, Dec. 2006, pp. 1281–1286, doi: 10.1109/ICIT.2006.372432.

[5] A. S. A. Mohamed, A. Gopinath, and M. R. Baiju, "A simple space vector PWM generation scheme for any general n-level inverter," *IEEE Trans. Ind. Electron.*, vol. 56, no. 5, pp. 1649–1656, May 2009, doi: 10.1109/TIE.2008.2011337.

[6] A. K. Gupta and A. M. Khambadkone, "A space vector PWM scheme for multilevel inverters based on two-level space vector PWM," *IEEE Trans. Ind. Electron.*, vol. 53, no. 5, pp. 1631–1639, Oct. 2006, doi: 10.1109/TIE.2006.881989.

[7] S. K. Gupta, Md. A. Khan, O. Singh, and D. K. Chauhan, "Simulation study of five-phase dual two level inverter system using unified space vector PWM," in *Proc. 10th IEEE Int. Conf. Commun. Syst. Netw. Technol. (CSNT)*, Jun. 2021, pp. 285–290, doi: 10.1109/CSNT51715.2021.9509593.

[8] G. C. Lim, H. Choi, and J. Ha, "Single phase commutation control of open-end winding PMSM fed by single DC-link dual inverter," in *Proc. 10th Int. Conf. Power Electron. ECCE Asia*, May 2019, pp. 2532–2537, doi: 10.23919/icpe2019-ecceasia42246.2019.8797190.

[9] A. S. Lutonin, A. Y. Shklyarskiy, and Y. E. Shklyarskiy, "Control strategy of dual fed open-end winding PMSM drive for traction applications," in *Proc. IEEE Conf. Russian Young Researchers Electr. Electron. Eng. (EIConRus)*, Jan. 2020, pp. 746–749, doi: 10.1109/EIConRus49466.2020.9039424.

[10] B. Li and C. Wang, "Comparative analysis on PMSM control system based on SPWM and SVPWM," in *Proc. Chin. Control Decis. Conf. (CCDC)*, May 2016, pp. 5071–5075, doi: 10.1109/CCDC.2016.7531902.

[11] R. Baranwal, K. Basu, and N. Mohan, "Carrier-based implementation of SVPWM for dual two-level VSI and dual matrix converter with zero common-mode voltage," *IEEE Trans. Power Electron.*, vol. 30, no. 3, pp. 1471–1487, Mar. 2015, doi: 10.1109/TPEL.2014.2316528.

[12] H. Ma, Y. Lu, K. Zheng, and T. Xu, "Research on the simplified SVPWM for three-phase/switches Y-type two-level rectifier," *IEEE Access*, vol. 8, pp. 214310–214321, 2020, doi: 10.1109/ACCESS.2020.3041283.

[13] A. Gopinath and G. A. S. Triangular, "3-D coordinate system for multi-level SVPWM generation," *IEEE Trans. Ind. Appl.*, vol. 56, no. 4, pp. 4061–4070, Jul./Aug. 2020, doi: 10.1109/TIA.2020.2995832.

[14] Q. Yan, Z. Zhou, M. Wu, X. Yuan, R. Zhao, and H. Xu, "A simplified analytical algorithm in abc coordinate for the three-level SVPWM," *IEEE Trans. Power Electron.*, vol. 36, no. 4, pp. 3622–3627, Apr. 2021, doi: 10.1109/TPEL.2020.3027742.

[15] Y. Zhou, S. Zhang, X. Cui, C. Zhang, and X. Li, "An accurate torque output method for open-end winding permanent magnet synchronous motors drives," *IEEE Trans. Energy Convers.*, vol. 36, no. 4, pp. 3470–3480, Dec. 2021, doi: 10.1109/TEC.2021.3083958.

[16] Y. Lee and J. Ha, "Hybrid modulation of dual inverter for open-end permanent magnet synchronous motor," *IEEE Trans. Power Electron.*, vol. 30, no. 6, pp. 3286–3299, Jun. 2015, doi: 10.1109/TPEL.2014.2325738.

[17] S. Lakhimsetty, N. Surulivel, and V. T. Somasekhar, "Improvised SVPWM strategies for an enhanced performance for a four-level open-end winding induction motor drive," *IEEE Trans. Ind. Electron.*, vol. 64, no. 4, pp. 2750–2759, Apr. 2017, doi: 10.1109/TIE.2016.2632059.

[18] W. Hu, C. Ruan, H. Nian, and D. Sun, "Simplified modulation scheme for open-end winding PMSM system with common DC bus under open-phase fault based on circulating current suppression," *IEEE Trans. Power Electron.*, vol. 35, no. 1, pp. 10–14, Jan. 2020, doi: 10.1109/TPEL.2019.2924821.

[19] M. Chen and D. Sun, "A unified space vector pulse width modulation for dual two-level inverter system," *IEEE Trans. Power Electron.*, vol. 32, no. 2, pp. 889–893, Feb. 2017, doi: 10.1109/TPEL.2016.2585223.

[20] W. Hu, C. Ruan, H. Nian, and D. Sun, "An improved modulation technique with minimum switching actions within one PWM cycle for open-end winding PMSM system with isolated DC bus," *IEEE Trans. Ind. Electron.*, vol. 67, no. 5, pp. 4259–4264, May 2020, doi: 10.1109/TIE.2019.2920618.

[21] X. Lin, W. Huang, and L. Wang, "SVPWM strategy based on the hysteresis controller of zero-sequence current for three-phase open-end winding PMSM," *IEEE Trans. Power Electron.*, vol. 34, no. 4, pp. 3474–3486, Apr. 2019, doi: 10.1109/TPEL.2018.2856372.

[22] A. P. Monteiro, C. B. Jacobina, F. A. D. C. Bahia, R. P. R. De Sousa, and N. S. D. M. L. Marinus, "Cascaded multilevel rectifiers for open-end winding PMSM," *IEEE Trans. Ind. Appl.*, vol. 58, no. 4, pp. 4873–4888, Jul. 2022, doi: 10.1109/TIA.2022.3168001.

[23] A. P. Monteiro, C. B. Jacobina, F. A. D. C. Bahia, and R. P. R. de Sousa, "Vienna rectifiers for WECS applications with open-end winding PMSM," *IEEE Trans. Ind. Appl.*, vol. 58, no. 2, pp. 2268–2279, Mar. 2022, doi: 10.1109/TIA.2022.3142658.

[24] L. Zhong and S. Hu, "Reference voltage self-equalization-based modulation strategy for open-end winding PMSM fed by dual three-level inverters with common DC bus," *IEEE J. Emerg. Sel. Topics Power Electron.*, vol. 10, no. 1, pp. 196–206, Feb. 2022, doi: 10.1109/JESTPE.2021.3069351.

[25] N. Chai and W. Hu, "Common-mode voltage suppression technique for open-end winding PMSM system with five bridge arms," *IEEE Trans. Energy Convers.*, vol. 37, no. 2, pp. 1499–1502, Jun. 2022, doi: 10.1109/TEC.2022.3156436.

[26] L. Xu and Z. Q. Zhu, "A novel SVPWM for open winding permanent magnet synchronous machine with extended operation range," *IEEE J. Emerg. Sel. Topics Power Electron.*, vol. 11, no. 1, pp. 901–914, Feb. 2023, doi: 10.1109/JESTPE.2022.3200346.

[27] H. Yao, Y. Yan, T. Shi, G. Zhang, Z. Wang, and C. Xia, "A novel SVPWM scheme for field-oriented vector-controlled PMSM drive system fed by cascaded H-bridge inverter," *IEEE Trans. Power Electron.*, vol. 36, no. 8, pp. 8988–9000, Aug. 2021, doi: 10.1109/TPEL.2021.3054642.

[28] K. Li and Y. Wang, "Maximum torque per ampere (MTPA) control for IPMSM drives using signal injection and an MTPA control law," *IEEE Trans. Ind. Informat.*, vol. 15, no. 10, pp. 5588–5598, Oct. 2019, doi: 10.1109/TII.2019.2905929.

[29] Q. An, J. Liu, Z. Peng, L. Sun, and L. Sun, "Dual-space vector control of open-end winding permanent magnet synchronous motor drive fed by dual inverter," *IEEE Trans. Power Electron.*, vol. 31, no. 12, pp. 8329–8342, Dec. 2016, doi: 10.1109/TPEL.2016.2520999.

SRINIVASAN PRADABANE was born in Puducherry, India, in 1983. He received the bachelor's degree from Pondicherry University, in 2005, the master's degree from Anna University, in 2008, and the Ph.D. degree from the National Institute of Technology Warangal (NITW), in 2016.

He did his postdoctoral research in the U.K., in 2018. He published many articles in reputable journals. His research interests include multi-level inverters, PWM schemes, induction motor drives, electric vehicles, integration of renewable, dc motor drives, BLDC drives, PMSM drives, LIM drives, propulsion technology for vehicles, measurement techniques, open-end winding drives, driver circuits, and digital control.

• • •

BERHANU DEGGEFA LEMMA was born in Diksis, Ethiopia, in 1988. He received the B.Sc. and M.Sc. degrees from Adama Science and Technology University, in 2012 and 2017, respectively.

From 2012 to 2019, he taught with Dire Dawa University, Ethiopia. He is currently a Research Scholar with the National Institute of Technology Warangal (NITW). He is also involved in PMSM drive. He has published journal and presented a paper at an international conference.